Full Length Article

Functionally graded structure of a nitride-strengthened Mg$_2$Si-based hybrid composite

Jeongho Yang [a,1], Woongbeom Heogh [b,1], Hogi Ju [b], Sukhyun Kang [c], Tae-Sik Jang [d,e],
Hyun-Do Jung [f], Mohammad Jahazi [g], Seung Chul Han [h], Seong Je Park [i], Hyoung Seop Kim [j,k,l],
Susmita Bose [m], Amit Bandyopadhyay [m], Martin Byung-Guk Jun [n], Young Won Kim [n],
Dae-kyeom Kim [o], Rigoberto C. Advincula [p,q,r], Clodualdo Aranas Jr. [s,*], Sang Hoon Kim [t,*]

[a] *School of Mechanical Engineering, Pusan National University, Busan 46241, Republic of Korea*
[b] *Department of Mechanical Design Engineering, Hanyang University, Seoul 04763, Republic of Korea*
[c] *Process Research 3 Team, LG Display Co., Ltd., Paju, Gyeonggi-do 10845, Republic of Korea*
[d] *Department of Materials Science and Engineering, Chosun University, Gwangju 61452, Republic of Korea*
[e] *Institute of Well-Aging Medicare & Chosun University LAMP Center, Chosun University, Gwangju 61452, Republic of Korea*
[f] *Division of Materials Science and Engineering, Hanyang University, Seoul 04763, Republic of Korea*
[g] *Department of Mechanical Engineering, École de Technologie Supérieure, Montreal, Quebec H3C 1K3, Canada*
[h] *Material & Component Convergence R&D Center, Korea Construction Equipment Technology Institute, Gunsan, Jeollabuk-do 54002, Republic of Korea*
[i] *School of Mechanical and Aerospace Engineering, Nanyang Technological University, Singapore 639798, Singapore*
[j] *Graduate Institute of Ferrous & Eco Materials Technology, Pohang University of Science and Technology, Pohang, Gyeongsangbuk-do 37673, Republic of Korea*
[k] *Advanced Institute for Materials Research, Tohoku University, Sendai 980-8577, Japan*
[l] *Institute for Convergence Research and Education in Advanced Technology, Yonsei University, Seoul 03722, Republic of Korea*
[m] *School of Mechanical and Materials Engineering, Washington State University, Pullman, Washington 99164, USA*
[n] *School of Mechanical Engineering, Purdue University, West Lafayette, Indiana 47907, USA*
[o] *Research Institute of Advanced Manufacturing Technology, Korea Institute of Industrial Technology, Incheon 21999, Republic of Korea*
[p] *Department of Macromolecular Science and Engineering, Case Western Reserve University, Cleveland, Ohio 44106, USA*
[q] *Department of Chemical and Biomolecular Engineering and Joint Institute for Advanced Materials, University of Tennessee, Knoxville, Tennessee 37996, USA*
[r] *Center for Nanophase Materials and Sciences, Oak Ridge National Laboratory, Oak Ridge, Tennessee 37830, USA*
[s] *Department of Mechanical Engineering, University of New Brunswick, Fredericton, New Brunswick E3B 5A3, Canada*
[t] *Power Generation Laboratory, Korea Electric Power Research Institute, Daejeon 34056, Republic of Korea*

Abstract

The *ex-situ* incorporation of the secondary SiC reinforcement, along with the *in-situ* incorporation of the tertiary and quaternary Mg$_3$N$_2$ and Si$_3$N$_4$ phases, in the primary matrix of Mg$_2$Si is employed in order to provide ultimate wear resistance based on the laser-irradiation-induced inclusion of N$_2$ gas during laser powder bed fusion. This is substantiated based on both the thermal diffusion- and chemical reaction-based metallurgy of the Mg$_2$Si–SiC/nitride hybrid composite. This study also proposes a functional platform for systematically modulating a functionally graded structure and modeling build-direction-dependent architectonics during additive manufacturing. This strategy enables the development of a compositional gradient from the center to the edge of each melt pool of the Mg$_2$Si–SiC/nitride hybrid composite. Consequently, the coefficient of friction of the hybrid composite exhibits a 309.3% decrease to –1.67 compared to –0.54 for the conventional nonreinforced Mg$_2$Si structure, while the tensile strength exhibits a 171.3% increase to 831.5 MPa compared to 485.3 MPa for the conventional structure. This outstanding mechanical behavior is due to the (1) the complementary and synergistic reinforcement effects of the SiC and

nitride compounds, each of which possesses an intrinsically high hardness, and (2) the strong adhesion of these compounds to the Mg_2Si matrix despite their small sizes and low concentrations.

1. Introduction

An automobile company requires a steering gear system (especially a pinion and rack) with customized features for high-performance vehicles and must be able to rapidly supply these parts without stocking them. The pinion and rack should have high wear resistance (regarding specific strength) in the sawtooth regions because these parts are directly linked to driver safety. Accordingly, Mg alloys are practical because of their high specific strengths derived from the presence of Mg, which has a high tensile strength of more than 100 MPa (alloying with Mg yields even higher strength and compatibility) as well as a significantly low density of 1.7 g cm^{-3} [1,2]. However, such alloys have poor thermal stability because of their low melting temperatures [3–5]. Additionally, because the ductilities of the Mg alloys are relatively low at room temperature, their forming methods and conditions are limited [5,6]. Moreover, as they are highly reactive with the surrounding oxygen or even nitrogen at high temperatures, a furnace chamber filled with inert Ar or SF$_6$ is necessary for heat treatment (HT) [7]. As such, Mg-based compounds (particularly Mg_2Si) can be used and operated at high temperatures (up to 1102 °C) and against external forces and pressures [8]. However, the anticipated engineering applications of this metal–metalloid compound will be continuously exposed to extreme conditions (high loads and temperatures), indicating that a further increase in its specific mechanical strength is essential even at high temperatures [8,9]. Various reinforcement materials, including BN, Si_3N_4, AlN, TiB_2, and ZrB_2, may be incorporated into the Mg_2Si matrix to maximize its specific thermomechanical strength [10–12].

Among many reinforcement materials, SiC has become a promising candidate owing to its extraordinary thermomechanical properties, which include a high elastic modulus (410 GPa), a low density (3.2 g cm^{-3}), and strong thermal stability (a melting temperature of 2730 °C) [12]. In particular, the SiC reinforcement within a Mg_2Si matrix can be used to impart high wear resistance, thereby rendering the surface more abrasive [13]. Moreover, the adequate mechanical strength (and, especially, the high wear resistance) of the resulting Mg_2Si–SiC composite can be further enhanced through the additional integration of other strong reinforcement materials [14]. In the present study, nitride compounds (Mg_3N_2 and Si_3N_4) are successfully formed through facile laser irradiation in an N_2 atmosphere [15]. By selecting a

functionally graded structure (FGS) and controlling the concentration ratio between the inert Ar and reactive N_2 gases in the environment during additive manufacturing, even higher strength can be achieved without sacrificing strain and elongation [16–18].

To illustrate the feasibility of laser powder bed fusion (LPBF) of this new type of Mg_2Si–SiC/nitride hybrid composite in an FGS for ultimate wear resistance, we applied the hybrid composite to the topological optimization of the pinion and rack used as core parts of a steering gear system. Furthermore, laser irradiation was conducted under an N_2 atmosphere to demonstrate the influence of the build direction during additive manufacturing (AM) on the wear resistance in the sawtooth and adjacent areas due to the localized generation of laser-irradiation-induced Mg_3N_2 and Si_3N_4 compounds as ternary and quaternary nitride reinforcement phases. From a microstructural perspective, the addition of a SiC reinforcement in the Mg_2Si matrix results in the localization of the secondary phase along the edges of the melt pools of the primary phase; in parallel, the strategy of controlling the concentration of Ar and N_2 during additive manufacturing enables the development of a compositional gradient from the centers to the edges of the melt pools of the Mg_2Si–SiC/nitride hybrid composite.

2. Experimental procedure

2.1. Additive manufacturing of the Mg_2Si structure, Mg_2Si–SiC composite, and Mg_2Si–SiC/nitride hybrid composite

Mg_2Si–SiC composite powder was prepared via gas atomization, as described in the Supplementary information. The Mg_2Si–SiC composite structure was additively manufactured with a layer thickness of 40 μm by applying a laser intensity of 75 W, a spot size of 80 μm, a hatching distance of 80 μm, and a laser speed of 60 mm s^{-1} [19]. For the various layers, the build rate ranged between approximately 5 and 20 cm^3 h^{-1} according to the structural compositions and as-built positions. Similarly, the nonreinforced Mg_2Si structure was built by applying identical laser parameters. The Mg_2Si–SiC/nitride hybrid composite structure was additively manufactured under a controlled concentration between Ar and N_2 in the mixture with a constant flow rate of 5 m^3 min^{-1}, especially for the steering gear parts (pinion and rack) with the compositionally

graded nitride layers in the specific regions. Thus, 13 layers of powder bedding and repeated laser irradiation were needed in order to fill the chamber with N_2. Then, all of the non-reinforced, composite, and hybrid composite structures were solid-solution-treated at 800 °C for 30 min, followed by rapid cooling to 25 °C within 10 min by gas quenching, then aging at 400 °C for 30 min, and slowly cooling to 25 °C in a furnace to (1) alleviate the residual and thermal stresses generated during laser irradiation and those accumulated from gas quenching in the solid-solution treatment, (2) lower the crystalline defects and mechanical flaws, and (3) transform the structures into a homogeneous microstructure in the matrix phase with tight bonding of the reinforcement materials.

2.2. Chemical characterization and physical evaluation of the Mg$_2$Si structure, Mg$_2$Si–SiC composite, and Mg$_2$Si–SiC/nitride hybrid composite

The amount of each element contained in the powder particles and as-built structures was measured using an inductively coupled plasma–optical emission spectrometer (ICP–OES; Optima 8300, Perkin Elmer, USA). Oxygen and carbon concentrations were determined using an oxygen/nitrogen analyzer (ON–900, Eltra GmbH, Germany) and a carbon/sulfur analyzer (CS–800, Eltra GmbH, Germany), respectively. The particle size distributions of each of the powders (Mg$_2$Si matrix powder, SiC reinforcement fragments, and Mg$_2$Si–SiC composite powder) were determined using a particle size analyzer (PSA; LS13 320, Beckman Coulter Inc., USA) equipped with a laser-driven scattering measurement detector. The morphologies of the precursor powder particles and microstructures of the AMed structures were studied using scanning electron microscopy (SEM; JSM–5800, JEOL, Japan). Electron backscatter diffraction (EBSD) analysis was carried out using a scanning electron microscope (SU70, Hitachi, Japan) equipped with an accessory (NordlysNano, Oxford, UK) to investigate the grain orientations of the structures before and after HT. Diffraction patterns and elemental compositions of the different regions of the as-built Mg$_2$Si–SiC/nitride hybrid composite were determined by selected area electron diffraction (SAED) and energy-dispersive X-ray spectroscopy (EDS) with transmission electron microscopy (TEM; JEM–ARM200F, JEOL, Japan). The crystalline phase changes in the powder particles and structures were determined via X-ray diffraction (XRD; D/Max–2500VL/PC, Rigaku International Corp., Japan) analysis at 40 kV and 250 mA over a 2θ range of 10–90°. The thermal behaviors of the Mg$_2$Si matrix powder, the SiC reinforcement fragments, and the Mg$_2$Si–SiC composite powder were measured using a differential scanning calorimeter (DSC; Q600, TA Instruments, USA) under a flow of Ar gas while heating at 10 K min^{-1}. The Vickers hardness values of the nonreinforced, composite, and hybrid composite structures were measured using a hardness tester (Duramin–40, Struers, Denmark) at a HV$_{0.5}$ loading force [16]. The Vickers hardness, using the HV$_{0.5}$ scale, was regulated according to the American Society for Testing and Materials (ASTM) E92–82 [16]. All of the as-built conventional,

composite, and hybrid composite structures additively manufactured using laser powder bed fusion (LPBF) were prepared for both tensile and compression testing by using a universal testing machine (Insight–100, MTS Systems, USA) at room temperature to compare the strengths of each structure before and after HT and under an identical crosshead speed of 2.0 mm min^{-1} [20]. A dry sliding wear test was conducted using a ball-on-disk tribometer (Ball/Pin on Disc, J&L Tech Co., Ltd., Republic of Korea) in air at room temperature. The surfaces of the specimens were polished prior to wear testing. The coefficient of friction (COF) of each structure was recorded during wear testing, and the scratch depth of each structure was measured using a three-dimensional (3D) profilometer (Contour GT–X, Bruker Corporation, USA) [21].

2.3. Governing equations of numerical simulations in laser powder bed fusion of the Mg$_2$Si–SiC composite

The heat-transfer and fluid-convection histograms of the Mg$_2$Si–SiC composite, additively manufactured via LPBF with either optimized or default laser-control parameters as a function of duration, were simulated using commercially available fluid dynamics analysis software (FLOW–3D, FLOW Science Inc., USA) [22–24]. The governing equations, including the conservation of mass, momentum, volume fraction, and thermal energy, in the LPBF process of the Mg$_2$Si–SiC composite are expressed as follows:

$$\frac{\partial \rho}{\partial t} + \nabla \cdot (\rho V) = \bar{M}, \tag{1}$$

$$\frac{\partial}{\partial t}(\rho V) + \nabla(\rho VV) = -\nabla P + \nabla\mu(\nabla V + \nabla V^T) + p_b + p_s, \tag{2}$$

$$\frac{\partial F}{\partial t} + \nabla \cdot (VF) = \bar{F}, \tag{3}$$

$$\frac{\partial}{\partial t}(\rho H) + \nabla \cdot (\rho VH) = \nabla \cdot (k\nabla T) + q_{pt} + q_l + q_{loss}, \tag{4}$$

where $\bar{M}$ is the mass source term (kg m^{-3} s^{-1}), ρ is the density (kg m^{-3}), V is the velocity (m s^{-1}), P is the pressure (Pa), μ is the viscosity (m^2 s^{-1}), p_b is the momentum term induced by buoyance force (N m^{-3}), p_s is the surface tension induced momentum (N m^{-3}), F is the fluid fraction, $\bar{F}$ is the fluid fraction change rate (s^{-1}), H is the enthalpy (J kg^{-1}), k is the thermal conductivity (W m^{-1} K^{-1}), q_{pt} is the phase transformation-induced heat source/sink term (W m^{-3}), q_l is the laser power source term (W m^{-3}), and q_{loss} is the heat loss term by convection and radiation (W m^{-3}) [22–24]. The fluid volume method was used to track the fluid-free surface, and the scalar F was employed to refer to the fluid fraction in the mesh cell [22]. For a specific fluid in a mesh cell, $F = 0$ indicates that this cell contains no fluid, whereas $F = 1$ indicates that this cell is entirely occupied by the fluid [22].

A mesh cell with an F value between 0 and 1 suggests a mixture with a specific amount of fluid [22]. Meanwhile, the liquid volume fraction (f_l) is determined as follows:

$$f_l = \begin{cases} 0 \ (T \leq T_s) \\ \frac{T - T_s}{T_l - T_s} \ (T_s < T < T_l), \\ 1 \ (T \geq T_l) \end{cases} \tag{5}$$

where T is the temperature applied to the composite (K), T_s is the solidus temperature (K), and T_l is the liquidus temperature (K) [25]. Thereafter, a damping force term is introduced to decrease the migration velocity of the liquid phase in the mushy zone during the phase transformation, which is described as follows:

$$p_{pt} = -A_{mushy} \frac{(1 - f_l^2)}{(f_l^3 + \delta_0)} V, \tag{6}$$

where A_{mushy} is the constant of the mushy zone (K m^{-3} s^{-1}), f_l is the liquid volume fraction, δ_0 is the small constant to avoid division by zero, and V is the migration velocity of the liquid phase (m s^{-1}) [22,23]. The enthalpy (H_{pt}) of the matrix in the composite in the solid-liquid mushy zone can be calculated using Eq. (7) as follows:

$$\Delta H_{pt} = H_{ref} + \int_{T_{ref}}^{T} c_p dT + f_l L, \tag{7}$$

where H_{ref} is the reference enthalpy (J kg^{-1}), c_p is the specific heat (J kg^{-1} K^{-1}), and f_l is the liquid volume fraction [22,23]. Following this, the phase transformation-induced heat source/sink term can be calculated as:

$$q_{pt} = -\frac{\partial}{\partial t}(\rho \Delta H_{pt}) - \nabla(\rho V \Delta H_{pt}), \tag{8}$$

where q_{pt} is the phase transformation-induced heat source/sink term (W m^{-3}), ρ is the density (kg m^{-3}), H_{pt} is the enthalpy (J kg^{-1}), and V is the migration velocity of the liquid phase (m s^{-1}) [20,21]. Keeping the simulation applying high energy to the Mg$_2$Si–SiC composite in mind, the laser power distribution in the numerical analysis area can be described as:

$$q = \frac{2\eta Q}{\pi r_s^2} \exp\left(-\frac{2w^2}{r_s}\right), \tag{9}$$

where q denotes the heat flux (W m^{-3}), η denotes the absorptance of the matrix in the composite, Q symbolizes the laser power (W), w indicates the radial distance from the beam center (m), and r_s denotes the laser spot radius (m) [20,21]. The given heat flux loss (q_{loss}) from the free surface is as follows:

$$q_{loss} = h_c(T - T_a) + \varepsilon\sigma(T^4 - T_a^4) + q_{evap}, \tag{10}$$

where h_c is the convective heat transfer coefficient (W m^{-2} K^{-1}), T_a is the ambient temperature (K), ε is the emissivity, σ is the Stefan-Boltzmann constant, and q_{evap} is the evaporation heat [22–24]. Assuming a heterogeneous mixture of metal vapor for simplicity, the evaporation heat (q_{evap}) is given as follows:

$$q_{evap} = \frac{0.01\Delta H_v^*}{\sqrt{2\pi MRT}} P_0 \exp\left(\frac{\Delta H_v^*(T - T_v)}{RTT_v}\right), \tag{11}$$

where H_v^* is the effective enthalpy of the metal vapor (J mol^{-1}), M is the molar mass (g mol^{-1}), R is the universal gas constant, P_0 is the atmospheric pressure (Pa), and T_v is the boiling temperature (K) [26]. The recoil pressure (P_{recoil}) is generated by LPBF above the evaporation temperature on the free surface of the matrix in the composite, and is expressed as follows:

$$P_{recoil} = 0.54P_0\exp\left(\frac{\Delta H_v(T - T_v)}{RTT_v}\right), \tag{12}$$

where the same indices given in Eq. (11) were used as the previous parameters used in the composite [24]. In addition, the Marangoni shear stress is induced by the spatial variation in the surface tension force:

$$\gamma = \gamma_m + \frac{d\gamma}{dT}\Delta T, \tag{13}$$

where γ is the surface tension at the surface temperature (N m^{-1}), T is the applied temperature (K), and γ_m is the surface tension at the melting temperature (kg s^{-2}) [24].

2.4. Finite element modeling of the Mg$_2$Si structure, Mg$_2$Si–SiC composite, and Mg$_2$Si–SiC/nitride hybrid composite

The FactSage 8.1 program was used to consider (1) the thermodynamic simulation based on the phase diagram, (2) the chemical decomposition of SiC within the Mg or Mg$_2$Si phases, (3) the effects of incorporating the reinforcements under an N$_2$ atmosphere across the FGS, (4) the thermal stability of the nitride compounds, and (5) the phase comparison in the presence or absence of the gas or liquid phases [27]. The compression behaviors of the Mg$_2$Si conventional, Mg$_2$Si–SiC composite, and Mg$_2$Si–SiC/nitride hybrid composite structures before HT were analyzed using a commercial finite element analysis (FEA) software package (Abaqus, Dassault Systèmes Simulia Corp., France), and the simulated stress-strain curves were compared to those obtained experimentally in the elastic regions [28].

2.5. Topological optimization for developing a more advanced steering gear system, complementary and synergistic incorporation of a lattice structure for additional mechanical stiffness, and strategic deposition of nitride compounds on the functionally graded structure for strong wear resistance

A 3D scanner (ZS–3040, Laser Design, USA) was employed to replicate the original pinion and rack used in the steering gear system of a vehicle. The original parts were fabricated using a combination of conventional manufacturing processes such as casting, forging, and machining. Thereafter, finite element modeling (FEM) was used to simulate the equivalent stress distributions on each of the original parts, and topological optimization was used to develop the newly designed parts that retained the stress-bearing regions of the original pinion and rack parts while eliminating the unnecessary stress-free regions. Meanwhile, an 800-μm

hatching-distance-controlled lattice structure was auxiliary-accompanied (deposited) inside the inner space of the topologically optimized pinion for maximizing the mechanical stiffness of a spatial structure, which exhibited a high mechanical stiffness exceeding a safety factor of 3.0, while minimizing the material usage to maintain the overhang design created to increase the fuel efficiency of the vehicle used in this study [13,27–29]. For the rack, the volume reduction was minimized for driver safety as the priority, even without considering the application of the supplementary lattice structure (Table 1).

3. Results and discussion

3.1. Simulations of heat transfer and fluid convection of the Mg_2Si–SiC composite additively manufactured via laser powder bed fusion with the optimized laser-control parameters

The heat transfer and fluid flow in the melt pools of the matrix in the Mg_2Si–SiC composite affect the track geometry and solidified microstructure [5,23]. The temperature gradient (G) and solidification rate (R_s) are two critical factors that determine the size and morphology of the melt pools over the solidified microstructure. Specifically, a higher G/R_s tends to produce finer melt pools in the microstructure, whereas the melt pool morphology changes from planar to cellular, and from columnar to equiaxial, as the G/R_s ratio decreases [5,23]. Based on these two fundamental principles, in the numerical analysis of the LPBF process for the Mg_2Si–SiC composite, the fluid dynamics of the melt pools exhibit Newtonian motion with laminar flow, depending on the Reynolds number [22]. Accordingly, the finite volume method is used to solve the governing equations in LPBF of the Mg_2Si–SiC composite. The enthalpy porosity method is also used to model the phase transformation during the liquefaction (melting) and solidification processes [22]. The flowability in the melt pools of the Mg_2Si–SiC composite is modeled in the CFD simulation. In the CFD parameters, the pre-determined physical properties of each Mg_2Si and SiC constituent are critical for the specific morphological transformations, diffusivity differences, chemical compositions, and distribution coefficients that significantly influence the thermal gradient and cooling rates of the melt pools [22]. Furthermore, the thermo-mechanical parameters of the composite can vary differently depending on the ambient temperature in the CFD simulation [22]. Consequently, the simulation is based on the corresponding thermomechanical and numerical variables (e.g., density, heat transfer coefficient, specific heat capacity, etc.) according to the ambient temperature, which is controlled by the laser intensity and speed, and the resulting thermal gradient and cooling rates of the melt pools are modeled [22]. The heat-transfer and fluid-convection simulations of the Mg_2Si–SiC composite that was additively manufactured via LPBF under the optimized laser-controlled parameters (a constant laser power of 75 W and a scan speed of 60 mm s^{-1}) produced steady-state melt pools without any mechanical flaws

such as pores, balling, and cracks (Fig. 1a–c). Therefore, the laser scan strategy prevented mechanical flaws and produced a smooth surface, even at the end of the track. However, the SiC reinforcement, which did not follow the aforementioned equations, was pushed out toward the edges of the semi-elliptical melt pools of the Mg_2Si matrix along the heat flow direction in the diffusive environment because of the buoyance effect during laser irradiation [12,30]. The results of a different set of heat-transfer and fluid-convection simulations in which the Mg_2Si–SiC composite was additively manufactured using LPBF under the default laser-control parameters (an abnormally high laser power of 150 W and a slow scan speed of 20 mm s^{-1}) are presented in Fig. 1d and e. The input of thermal energy during laser irradiation creates a Marangoni flow on the surface of each melt pool, and the extent of the buoyancy force is determined by the Marangoni flow and the ambient temperature [31,32]. The effect of the buoyancy force can be analyzed by using the equation of motion in the CFD simulation, although the pores are formed when the flowing gas is trapped suddenly in the melt pools during the gas quenching process after laser irradiation [31,32]. The buoyancy force is determined by the coefficient of thermal expansion according to the ambient temperature, and the pores are created by the flowing gas becoming trapped in the melt pools under equilibrium collapse due to the imbalance between the upward buoyancy force and the downward pressure from the flowing gas [31,32]. Furthermore, the pore size increases as the extent of this imbalance increases [31,32]. The results were two-dimensional (2D) cross-sectional histograms of the single laser-scanned track of the Mg_2Si–SiC composite seen from either the longitudinal or transverse directions with each temperature gradient field as a function of time when intentionally misguiding the laser-control parameters [31,32]. The melt pool dynamics of the Mg_2Si–SiC composite became unsteady, and pores and cracks were abundant, even at the start of the track, depending on their positions within the melt pools because of the substantial temperature variation (resulting in evaporation and spatter formation of the constituents) [31,32]. The overheating caused by the abnormally high laser power and slow scan speed created keyholes because the laser imparted excess energy to the melt pools during the following two processes [31,32]. First, the formation of pores proceeded via rapid collapse owing to vapor depression on the surface of the laser-scanned track [31,32]. Second, the inert Ar gas became trapped within the liquid metal, with the lagging shape flowing into the pores, thereby rapidly solidifying the melt pools [31,32]. Based on these simulations, AM of the Mg_2Si-based matrix incorporated with the SiC reinforcement was completed in practice, but the process was challenging due to spattering of the evaporated Mg and Si.

3.2. Microstructural comparison of the nonreinforced, composite, and hybrid composite structures additively manufactured before and after heat treatment

As deduced from the specific microstructures in Fig. 2d, although the heat generated by the LPBF process flowed di-

Table 1
A reference comparison of the physical and chemical properties of our Mg$_2$Si–SiC/nitride hybrid composite with those of the conventional and composite structures fabricated by common casting, welding, spraying, etc., evaluated and classified in terms of alloy design and specific strength.

Manuf. process	Alloy system	Specific applications	Manuf. advantages	Mechanical properties	Advantageous physical properties	Key points	Ref. (No.)
LPBF	Mg$_2$Si–SiC/nitride hybrid composite	An FGS is obtained in the intended regions while constructing a pinion-and-rack steering gear system	This can be built as a delicate structure with a high strength and low density	A tensile strength of 831.5 MPa after HT	The coefficients of friction of the AMed hybrid composite and the heat-treated hybrid composite were –1.13 and –1.67, respectively, which represent significant decreases compared to that of the heat-treated conventional structure (i.e., –0.54)	The formation of a CGD in the microstructure and an FGS along with the build direction	Our study
Ultrasonic casting	Mg$_2$Zn SiC composite	No specific applications	Achieving a uniform dispersion of dense SiC nanoparticles in the Mg matrix	The Mg$_2$Zn composite with SiC exhibits a compression strength of 410 MPa compared to 50 MPa for the conventional structure without SiC	At 400 °C, the Mg$_2$Zn composite with 14 vol.% SiC had a tensile strength of 150 MPa	The ultrahigh-performance, light-weight and strengthened composite can improve the energy efficiency and system performance in numerous applications	[8]
Powder bed fusion	A bioinspired Ti–6Al–4V lattice structure infiltrated with Mg (Mg–Ti composite)	No specific applications	The strength of the composite was enhanced via Mg-melting infiltration	The Mg–Ti composites exhibited tensile strengths of 156.6–226.6 MPa, compared to 12.2–65.4 MPa in the absence of Mg	The interpenetration of the Mg and Ti–6Al–4V components in the 3D structure allows for the effective transfer of stress within and between each phase, thereby conferring the reinforcement with a high strengthening efficiency	The deformation and cracking of the relatively weak Mg phase can be restricted and retarded by the stronger Ti–6Al–4V component, thereby retarding the mutual partitioning of the components within the composite	[47]
Selective laser melting and ball milling	Carbon nanotube–AZ31B composite	No specific applications	Highly typical and conventional fabrication techniques applied	Tensile strengths ranging from 264 to 286 MPa according to the laser input energy density	The morphology and porosity of the melt pools controlled according to the laser input energy density, thereby enhancing the tensile strength of the composite	The melt pools of the composite were simulated based on the temperature distribution of each constituent and the interactions between the carbon nanotube reinforcements and the AZ31B alloy	[15]

Table 1 (*continued*)

| Manuf. process	Alloy system	Specific applications	Manuf. advantages	Mechanical properties	Advantageous physical properties	Key points	Ref. (No.)
Various techniques and methods	Mg–graphene and Mg–carbon nanotube composites	Various applications mentioned	The appropriate manufacturing methods can be matched to the desired applications	Tensile strengths ranging from 150 MPa to 500 MPa	As high a strength as possible	Their high strengths were explained by the intensities and extents of physiochemical interactions between the Mg alloys and the graphene and carbon nanotube reinforcements depending on the fabrication processes applied	[48]
Nanoparticle dispersion and wetting are provided by the cavitation and streaming effects due to ultrasonic vibration of the Mg melt	AZ91/SiC + TiC	No specific applications indicated	Various, depending on the techniques and methods applied in the fabrications	Depending on the constituents and concentrations of the matrices and reinforcements, the tensile strengths ranged from 191 MPa (AZ91/SiC) up to 397 MPa (AZ91/SiC + TiC)	As high a strength as possible	The results are explained based on the grain refinement strengthening mechanism, the Orowan strengthening mechanism, the Taylor strengthening mechanism, and the load transfer mechanism	[11]
A series of extrusion, heat treatment, and rolling processes	Mg–Li-based alloy (no composite)	No specific applications	The water-quenched and 70 °C aged alloy exhibited excellent ductility during rolling, achieving strains of over 80% without cracking	The specific strength and elongation and strain were significantly enhanced with the optimized amount of Li addition	Good strength-to-weight ratio (specific strength)	The Mg–Li-based alloy was designed for an ultralow density (1.4 g cm^{-3}), and was strong, ductile, and more corrosion resistant than the conventional Mg-based alloys reported so far	[3]
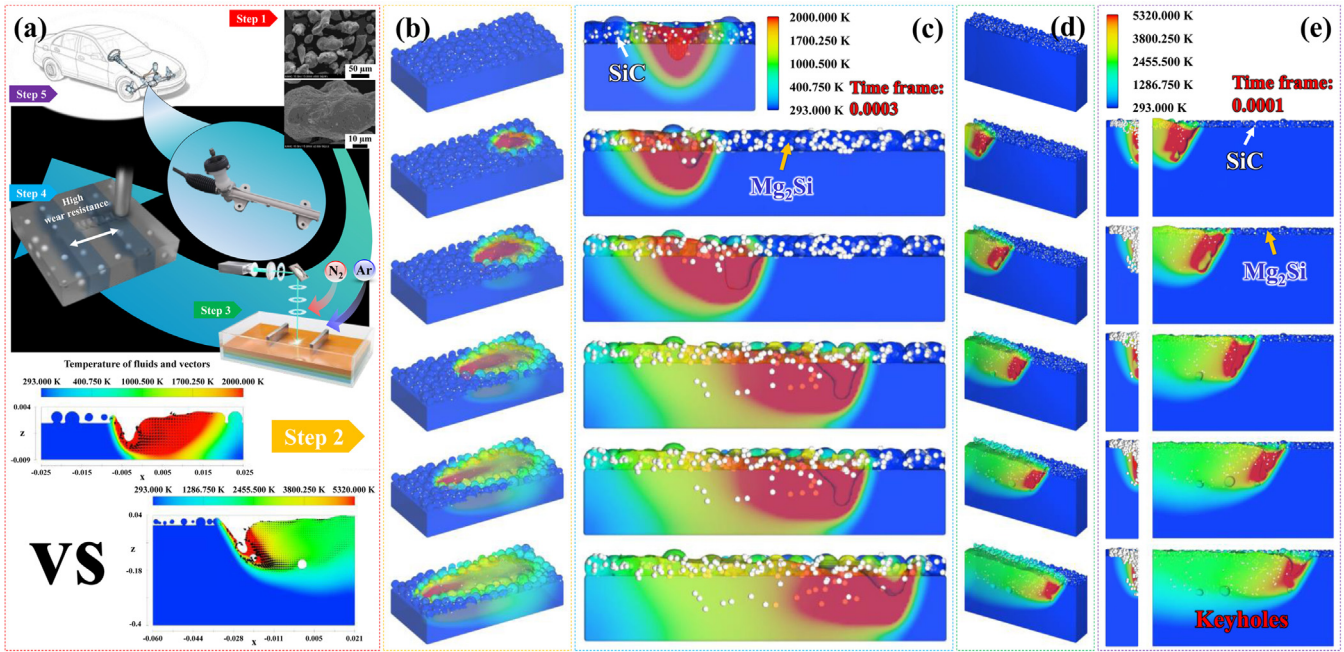
Fig. 1. (a) Schematics of the LPBF process for the nitride-strengthened Mg_2Si–SiC-based hybrid composite with the FGS. (b) A 3D view of the single laser-scanned track on the Mg_2Si–SiC composite with the temperature gradient field. (c) 2D cross-sectional histograms of the single laser-scanned track on the Mg_2Si–SiC composite seen from either the longitudinal or transverse directions with each temperature gradient field as a function of time. (d) A 3D view of the single laser-scanned track on the Mg_2Si–SiC composite with the temperature gradient field when the abnormally high laser power of 150 W and slow scan speed of 20 mm s^{-1} were applied in the LPBF process. (e) 2D cross-sectional histograms of the single laser-scanned track of the Mg_2Si–SiC composite seen from either the longitudinal or transverse directions with each temperature gradient field as a function of time when intentionally misguiding the laser-control parameters.

rectly along the Mg_2Si matrix, the thermal energy flow was suppressed by the SiC reinforcement with its lower thermal conductivity, during which the presence of melt pools became less distinct than those of the nonreinforced Mg_2Si structure (Fig. 2a–c). Hence, the composite had a high thermal energy concentration, which could potentially form less bonding along the interfacial boundaries between the matrix and reinforcement phases, attracting significant residual and thermal stresses accumulated along the secondary reinforcement phase (Fig. 2e). This phenomenon was primarily caused by higher densities of voids, dislocations, and defects at the interfacial boundaries between the two phases, reducing strain and elongation [12,30]. However, if the secondary phase was tightly conjugated to the primary phase solidified from the highly diffusive environment during laser irradiation, then the abrasive wear load associated with the mechanical strength would have been effectively resisted throughout SiC embedded along the melt pools without their withdrawal from Mg_2Si, thereby maintaining the persistence of the melt pools and inducing the reinforcement effect [12,19,30,33]. As shown in Fig. 2f and g, the equiaxial dendrites in the top plane, along with the columnar dendrites in the side plane (which together comprised the secondary SiC and other nitride compounds embedded in the Mg_2Si matrix phase), were all present, with overlapping connections between the identical fluid and fan-shaped melt pools. The nitride compounds did not affect the microstructures because of their small sizes and low concentrations. Moreover, after HT (solid-solution treatment followed

by aging), all the melt pools disappeared from both the top and side planes of the microstructures (Fig. 2h–m), leaving only the reinforcement phases comprising SiC, Mg_3N_2, and Si_3N_4 without thermal decomposition throughout Mg_2Si. For the matrix, smaller equiaxial dendrites were developed over the microstructures irrespective of the top or side planes; in particular, the continuous and high-temperature environment provided tighter bonds between the matrix and reinforcement phases.

3.3. Comparison of electron backscatter diffraction analysis results of the additively manufactured Mg_2Si–SiC/nitride hybrid composite before and after HT

Before HT, the low-angle grain boundaries (LAGBs; $1° < \theta < 5°$), distinct phase constituents, and crystallographic distortions were clearly revealed by the contrasting color micrographs of the Mg_2Si–SiC/nitride hybrid composite in Figs. 3a–n. First, the red-lined regions indicate the presence of highly dense LAGBs (1.45 cm in length with an overall length of 4.62 cm) aligned predominantly along the grains. Furthermore, the map demonstrates more elongated grains of the matrix perpendicular to the direction of laser irradiation, indicating that the epitaxial grains grew in a columnar manner [34,35]. As observed in the microstructure, these features were primarily induced by the artificial incorporation of the reinforcement phases (SiC, Mg_3N_2, and Si_3N_4), as revealed in the high-magnification microscopic analysis. Subsequently,
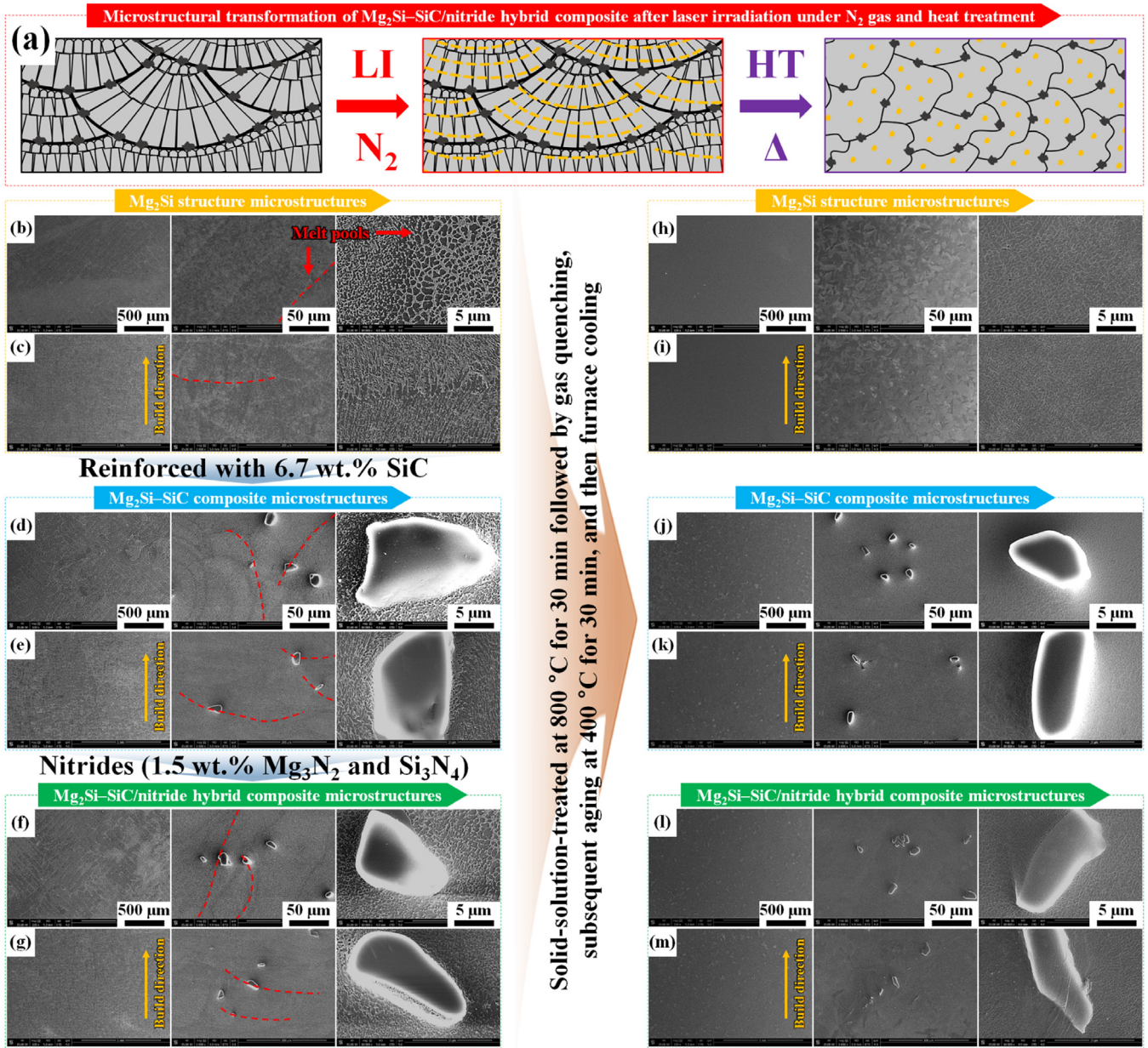
Fig. 2. (a) Schematics of the microstructural transformation from the Mg₂Si structure, through the Mg₂Si–SiC composite, to the Mg₂Si–SiC/nitride hybrid composite. SEM images of the microstructures in (b) the top and (c) the side planes of the AMed Mg₂Si structure. SEM images of the microstructures in (d) the top and (e) the side planes of the AMed Mg₂Si–SiC composite. SEM images of the microstructures in (f) the top and (g) the side planes of the AMed Mg₂Si–SiC/nitride hybrid composite. SEM images of the microstructures of (h, i) the Mg₂Si structure, (j, k) the Mg₂Si–SiC composite, and (l, m) the Mg₂Si–SiC/nitride hybrid composite after subsequent HT.

the as-printed hybrid composite that was developed with the elongated grains spread out from the centers to the edges of the melt pools perpendicular to the direction of laser irradiation in the inverse pole figure (IPF) map, which is commonly observed in the side-plane microstructure of the AMed structure [36]. However, considering the similarity to the crystallographic orientation of each grain in the as-printed Mg₂Si conventional structure (Figure S3), the grain orientations in the matrix of the hybrid composite were highly associated with the (0 0 1) and (1 1 1) planes of the matrix, which was mainly composed of elongated grains. By contrast, in certain specific regions, the equiaxial grains with the preferred (1 1

0) plane were predominant, especially in the peripheral areas of the reinforcements (mostly for the microscale SiC reinforcement rather than the nanoscale nitride reinforcements), in which heat flow was prevented due to the presence of ceramic reinforcements with lower thermal conductivity values [19,36]. As a result, the EBSD analysis helped to determine the crystallographic distortions that occurred predominantly at the grain boundaries with the high density of LAGBs, especially between the (0 0 1), (1 1 0), and (1 1 1) planes of Mg₂Si and the (1 0 − 1 0) plane of SiC. However, after HT (solid-solution and subsequent aging treatments), the inhomogeneous microstructure comprising the melt pools and
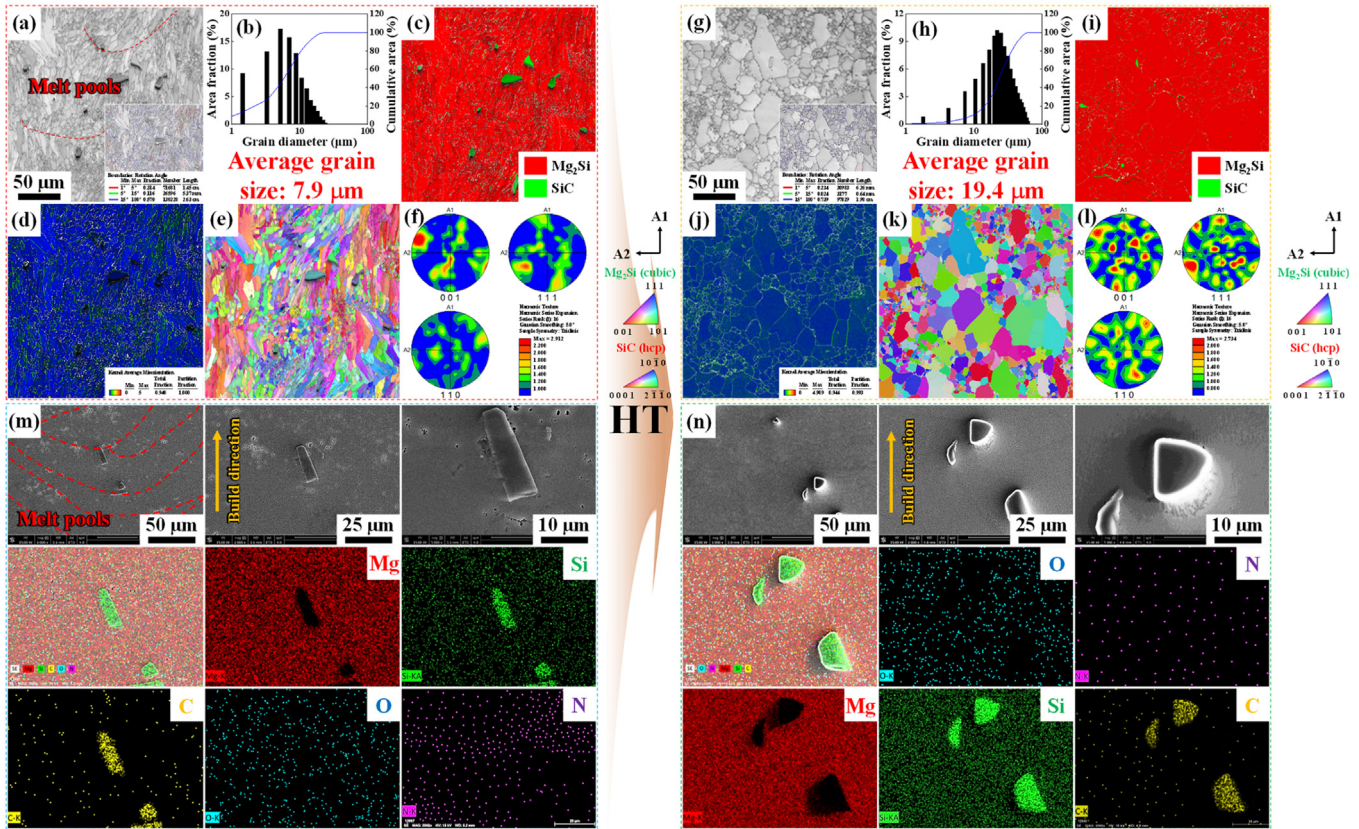
Fig. 3. (a, g) The IQ maps with the insets of grain boundary maps (red: < 5° boundary; green: > 5° and ⟨ 15° boundaries; blue: ⟩ 15° boundary) and (b, h) the grain size distributions of the Mg$_2$Si–SiC/nitride hybrid composite before and after HT. (c, i) The phase maps, (d, j) the kernel average misorientation maps (color contrast images from blue to red according to the misorientation density), (e, k) the IPF maps, and (f, l) the pole figures (f and l for the Mg$_2$Si with the antifluorite structure) of the Mg$_2$Si–SiC/nitride hybrid composite before and after HT. (m) The SEM images and corresponding elemental mapping images of the Mg$_2$Si–SiC/nitride hybrid composite before HT, revealing that the Mg$_3$N$_2$ and Si$_3$N$_4$ reinforcements were distributed around the melt pools of the Mg$_2$Si matrix irrespective of the presence or absence of the SiC reinforcement. (n) Following HT, the nitride compounds were uniformly spread out and became homogeneously distributed, as shown in the corresponding nitrogen mapping image. (For interpretation of the references to colour in this figure legend, the reader is referred to the web version of this article.)

elongated grains disappeared, and the morphology was refined, with an average grain size of 19.4 µm, irrespective of their locations at the centers or edges of the erstwhile melt pools. The fraction of the LAGBs, which was associated with the crystallographic distortions and were primarily present at the interfacial boundaries between the matrix and reinforcement phases, significantly decreased [18,37]. A less preferred texture was present in the IPF map, and the measured texture intensity index was 1.31, which denotes a microstructure with a weak texture [17,35,37]. Owing to a lack of a strong texture, the grains adopted a much more equiaxial morphology, accompanied by the transformation of a small number of fine equiaxial grains to larger equiaxial grains [19].

3.4. Differentiation between the functionally graded structure and compositional gradient distribution in the Mg$_2$Si–SiC/nitride hybrid composite

The microstructure of the Mg$_2$Si–SiC/nitride hybrid composite with the FGS of nitride compounds in the intended regions, which is highly applicable to a bimodal structure that requires the dual functionality provided by the differ-

ent chemical compositions according to the as-built positions, is depicted in Fig. 4c. In detail, the specific layers composed of the nitride compounds were combined in each step through a gradual transition from an Ar atmosphere to an N$_2$ atmosphere to obtain a graded structure. This graded structure contained the Mg$_2$Si–SiC composite, followed by a series of discrete compositional mixtures with a layer thickness of 40 µm (featuring less-nitride-generated layers and more nitride-containing layers) in the middle and ended with the Mg$_2$Si–SiC/nitride hybrid composite [14,16,38]. After surface polishing and etching, the FGS displayed a similar microstructure to that of the conventional structure (Fig. 4a) without the reinforcements, and that of the composite without the nitride reinforcements (Fig. 4b) in the low-magnification microscopic analysis, primarily owing to their small sizes and low concentrations. Furthermore, the nitride compounds were present, from the centers to the edges of the melt pools over the microstructure, as another type of graded structure owing to the exposure to N$_2$ gas during laser irradiation (Figure S6). This resulted in the formation of a compositional gradient distribution (CGD) in the intended region of the hybrid composite. In particular, the defects caused by consti-
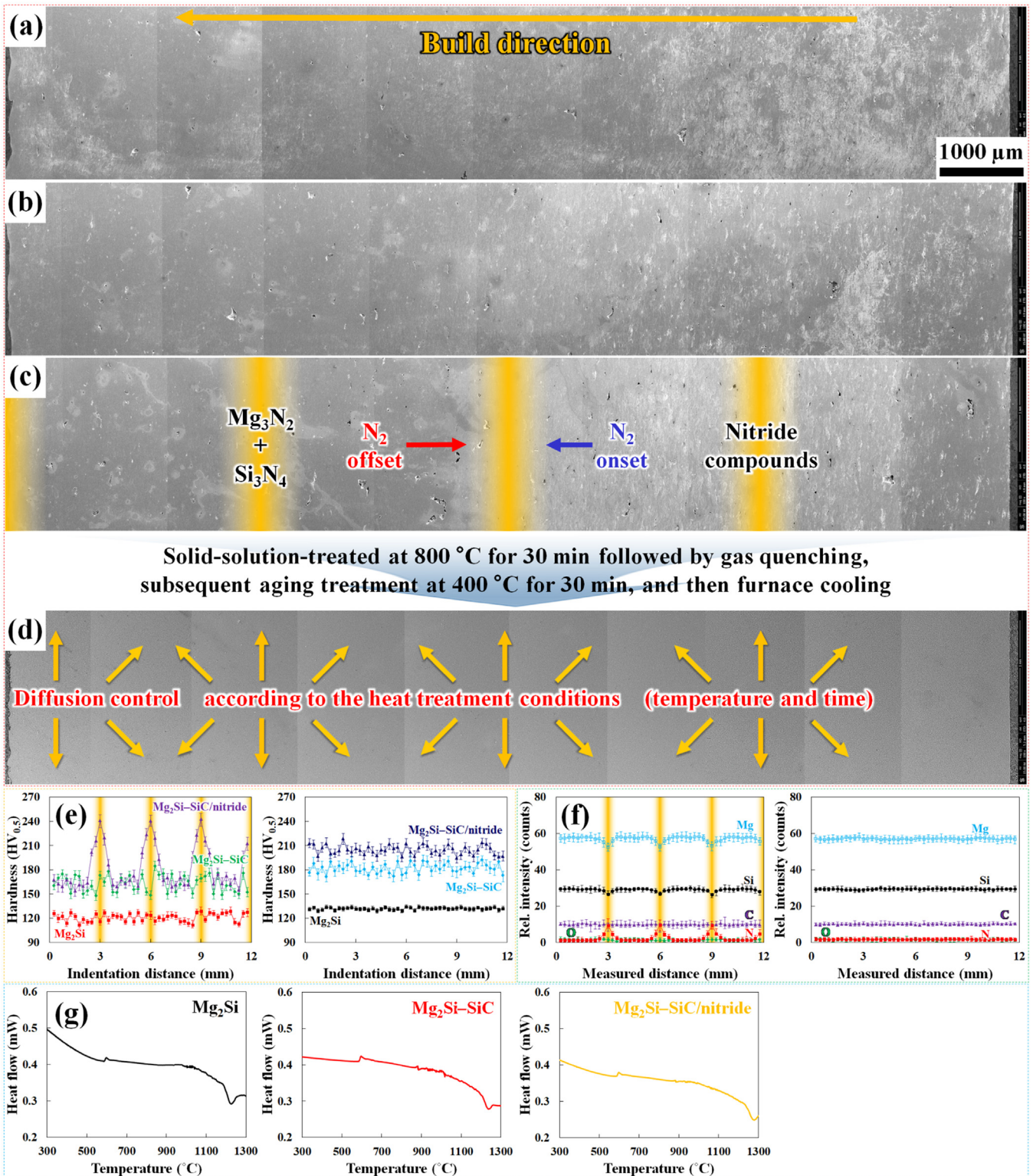
Fig. 4. Panoramic SEM images of (a) the Mg$_2$Si structure, (b) the Mg$_2$Si–SiC composite, and the Mg$_2$Si–SiC/nitride hybrid composite before (c) and after (d) HT. The selective laser melting process for fabricating the Mg$_2$Si–SiC/nitride hybrid composite was conducted in a controlled N$_2$ atmosphere to allow the formation of nitride compounds within the as-built interval of 1 mm. During HT, the Mg$_2$Si matrix provided the continuous and high-temperature environment for the dispersion of the nitride compounds, but not for the distinct rearrangement of the SiC reinforcement. (e, f) A comparison of the Vickers hardness values and chemical compositions along the build direction from the bottom to the top of the as-built Mg$_2$Si–SiC/nitride hybrid composite that was additively manufactured before and after HT. (g) The DSC scans of the Mg$_2$Si structure, Mg$_2$Si–SiC composite, and Mg$_2$Si–SiC/nitride hybrid composite.

tutional supercooling, residual and thermal stress concentrations, and coefficients of thermal expansion at the interfacial boundaries between the dissimilar nitride layers of the hybrid composite were alleviated by the gradual changes in the nitride deposition layers within the FGS, which has various crystalline defects such as voids, dislocations, and stacking faults [14,16,39]. Specifically, the number of defects at the interfacial boundaries between the fewer nitride-generated layers with low strength but high strain and the greater nitride-generated layers with high strength but low strain decreased to a greater extent compared to those in a straightly bound hybrid composite that was formed directly or bound thoroughly through a sudden transformation [33,39]. Since there are some slight differences in the coefficients of thermal expansion between the Mg_2Si metallic matrix (13×10^{-6} K^{-1}) and the SiC ceramic reinforcement (4.5×10^{-6} K^{-1}) at 25 °C, this might have a weak adverse effect and might lead to the generation of residual and thermal stresses at the interface [40,41]. A difference in the residual and thermal stresses can result in either contraction or expansion, which leads to unstable bonding at the interface and, hence, some damage or weakness over the Mg_2Si–SiC composite, especially during the selective laser melting process [40,41]. Nevertheless, the similarity between the coefficients of thermal expansion provides positive advantages in terms of strength and stability at the interface for the following reasons: (1) both the Mg_2Si matrix and SiC reinforcement are covalent compounds, and are therefore insensitive to the slight differences in the coefficient of thermal expansion, (2) the Si–Si interaction between the Mg_2Si matrix and SiC reinforcement can provide strong interconnections, (3) the gas quenching process after laser irradiation provides a clean interface with no voids, dislocations, or other defects, thereby indicating strong interfacial bonding before any microstructural damage or weakness can occur due to the concentration of residual thermal stresses, (4) although the distinctive interface is more vulnerable to external impact than is the internal morphology, the morphologies at the interfacial boundaries are irregular rather than smooth and spherical, and can therefore act to straighten the propagation of cracks and fractures and further reduce the strain and elongation, and (5) due primarily to the strong suppression of nucleation formation and grain growth, the rapid solidification process allows the dendrites in the Mg_2Si matrix adjacent to the SiC reinforcement to become smaller. In this study, we employed AM to construct an FGS with 25 layers per level of compositional transition (a layer thickness of 40 μm, and thus, a total of 25 layers, all of which were 1 mm in length) to minimize the residual and thermal stresses at each interfacial region. Fig. 4e displays the Vickers hardness measurement results of the FGS for each chemical constituent as the Mg_2Si–SiC composite transforms to the Mg_2Si–SiC/nitride hybrid composite. Although almost constant hardness values were obtained for the stable Mg_2Si–SiC composite, a sudden three-fold increase was observed in specific regions where N_2 gas was inserted during laser irradiation; otherwise, the hardness values stabilized when Ar gas was reinserted, compared to those of the Mg_2Si–SiC composite laser-irradiated only under the Ar atmosphere. In particular, the measured maximum Vickers hardness value for the hybrid composite additively manufactured in the N_2 atmosphere was 242.8 $HV_{0.5}$ owing to the generation of these brittle phases (Mg_3N_2 and Si_3N_4). The chemical compositions of the entire microstructure according to the as-built positions of the hybrid composite (including the FGS) are shown in Fig. 4f. Although there were several errors in the EDS analysis, the molecular percentages of each constituent element, even including the nitride compounds, in the specific regions exhibited a sudden three-fold increase with each 1-mm band thickness [14,38]. Thus, the as-built positions adequately matched the indentation locations created during the previous hardness measurements, which indicated the significant correlations between the chemical compositions and hardness measurements [14,42]. Following HT, the molecular percentages of the nitride compounds in the chemical composition of the hybrid composite without the FGS slightly increased owing to the distribution over the microstructure.

The microstructural examination of the microscale SiC- and nanoscale nitride-reinforced Mg_2Si matrix (Mg_2Si–SiC/nitride) was performed using TEM. Figs. 5a–c illustrate low-magnification TEM images of the hybrid composite. These images show that the SiC reinforcement (the darker area) is retained within the Mg_2Si matrix (the lighter area) with a clean interface containing no voids, dislocations, or other defects, thus indicating strong interfacial bonding [19,30]. Simultaneously, a trace of the active wetting of the matrix near the reinforcement was found at the interface between Mg_2Si and SiC, as shown in Fig. 5c. This is because the high thermal energy provided by the laser irradiation process did not melt the SiC phase, but completely melted the Mg_2Si phase at the interface, which explains the strong diffusion reaction of Mg_2Si in the LPBF process [19,34,36]. Furthermore, regardless of the envisaged nucleation of the matrix, the stabilizing energy at the interface of the reinforcement caused the occurrence of a certain orientation of Mg_2Si, which was significantly limited by the interactions between Mg_2Si and SiC (despite having Si in both phases), and thus might interconnect through the Si–Si interaction [35]. The microstructure of the matrix demonstrates that strong diffusion followed by sudden cooling occurred at the interface between Mg_2Si and SiC, which is the unique characteristic of the laser HT [21,33]. However, despite the use of such a high-temperature reaction, there was no thermal degradation of SiC along with Mg_2Si, as demonstrated by the SAED analysis at the interfacial boundary (Fig. 5g). To evaluate the morphological features, heterogeneous distributions, and chemical states of the nitride compounds (reinforcements) in the Mg_2Si–SiC/nitride hybrid composite, TEM images, SAED analyses, lattice fringe measurements, and EDS mapping scans were also performed, as illustrated in Figure S6. As previously mentioned, each graded structure was distributed in the nitrides from the centers to the edges of the melt pools throughout the microstructure, including several melt pools of the AMed hybrid composite. The SAED patterns in each specific region near the melt pools revealed the overlapping presence of Mg_3N_2, α-
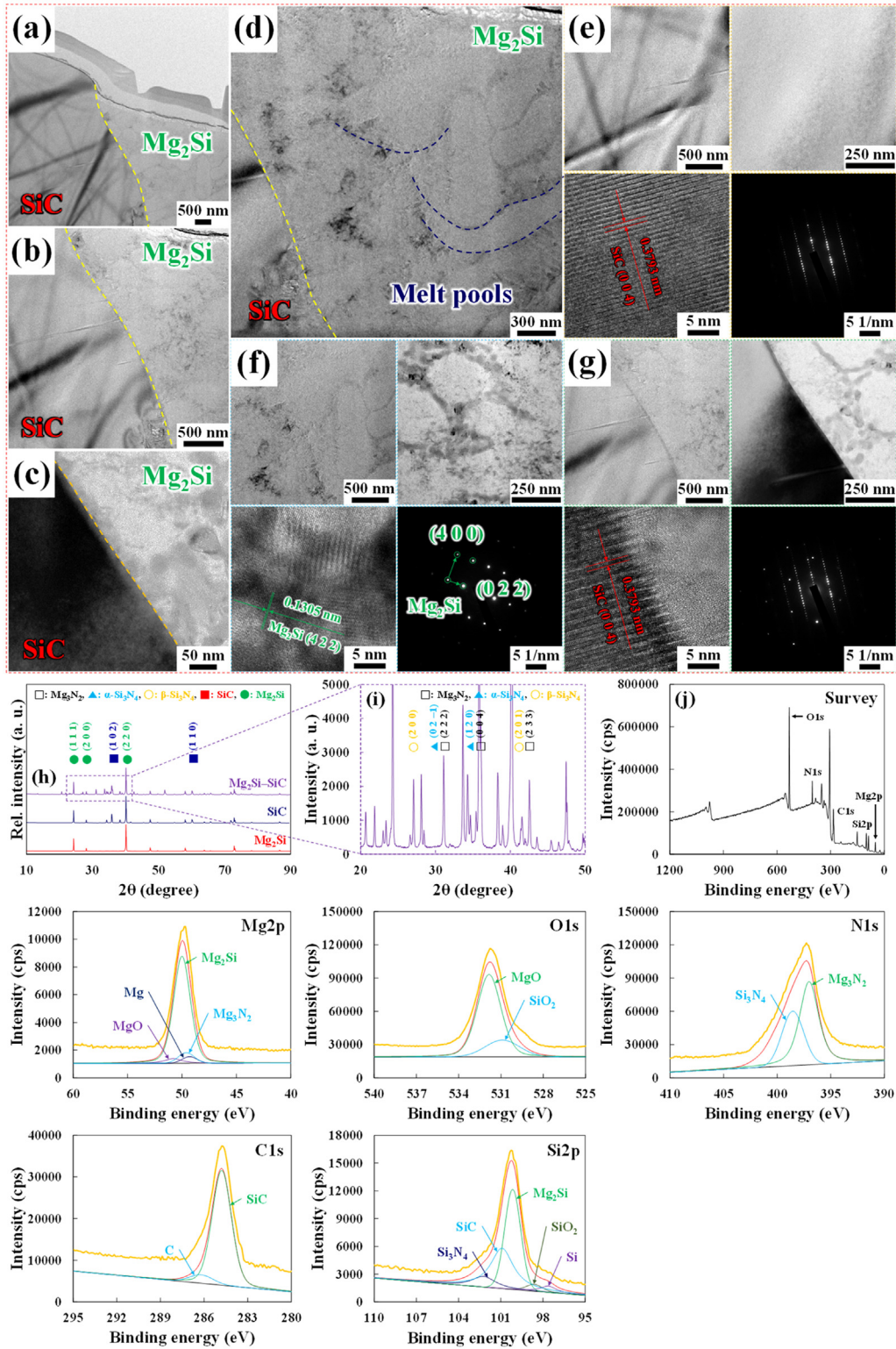
Fig. 5. (a) The TEM image of the primary Mg_2Si matrix with the antifluorite structure alongside the secondary SiC reinforcement with the hexagonal close-packed structure. The Mg_3N_2 and Si_3N_4 (comprising both α-Si_3N_4 and β-Si_3N_4) reinforcements of several tens of nanometers of diameters were spread out in the gradient distribution within each hemi-elliptical melt pool of the Mg_2Si matrix, identical to the observations in the SEM analysis. (b) The low-magnification TEM image, (c–g) the intermediate-magnification TEM images, and (e–g) the high-resolution TEM images, along with the corresponding lattice fringe measurements and SAED patterns, of (f) the primary matrix phase and (e) the secondary reinforcement phase. (f, g) The nitride compounds were mostly formed by the nitridation of the Mg_2Si matrix under N_2 rather than from the decomposition of the SiC reinforcement because the Mg_3N_2 and Si_3N_4 phases were mostly present in the matrix, while the microstructure of the SiC phase did not show any evidence of decomposition. (h–j) Although a sufficiently large amount of the secondary SiC phase was evident in the primary Mg_2Si phase, there were no additional unexpected peaks, thereby confirming that no chemical reactions occurred between these two phases, at least according to the XRD and XPS analysis results.

Si_3N_4, and β-Si_3N_4 (Figure S6c of Mg_3N_2 compared to Figures S6d and S6e of α-Si_3N_4 and β-Si_3N_4). All the three patterns conform to the spot and dot patterns, which explain all the nitride compounds broadly (distributed) scattered with their small sizes adjacent to the molten Mg_2Si matrix in the hybrid composite. A number of specific directions existed in the Mg_2Si–SiC/nitride hybrid composite. Thus, while the lattice spacing of 0.1305 nm indicated the Mg_2Si phase with the [4 2 2] direction, the average lattice spacing of the marked area was 0.3793 nm, which indicated that the SiC compound had the [0 0 4] direction. Thus, the SAED pattern shows that the Mg_2Si phase has an orientational relationship of (4 2 2)$_{Mg2Si}$//(0 0 4)$_{SiC}$ with the SiC phase. In addition, the presence of the reinforcement in the matrix was more definitely identified by its SAED pattern. Thus, at the interfacial boundary between the Mg_2Si and SiC phases, the SAED pattern had a zone axis of [0 1 1]. In Fig. 5e–g, the selected spots indicate the (4 0 0), (0 2 2), and (4 2 2) planes of Mg_2Si and the (0 0 4), (0 1 2), and (0 1 6) planes of SiC. However, there were no electron diffraction patterns for the residual presence of graphite and Si derived from the decomposition of the SiC phase, which demonstrated that SiC was successfully retained, thereby maintaining the high wear resistance of the hybrid composite even under the high-temperature environment during laser irradiation. In other words, no new peaks appeared at the interfacial boundaries between the reinforcement and matrix phases, thereby indicating that no chemical reactions occurred between them, and no unexpected compounds or impurities were observed, even under high-energy laser irradiation. Furthermore, the high-angle annular dark-field (HAADF) images and corresponding EDS mapping analysis results indicated that all the nitride compounds were formed because of the thermal decomposition of Mg_2Si, as opposed to that of SiC, under laser irradiation in the N_2 atmosphere owing to the high thermal stability of SiC (which helped in maintaining the high wear resistance imparted by the reinforcement) [19–21,30–36].

3.5. Enhanced mechanical strength of the hybrid composite

As shown in Fig. 6, despite a slight increase in the density, the tensile and compressive strengths of the nonreinforced, composite, and hybrid composite structures increased significantly because of (1) the increase in the amount of SiC and nitride reinforcements, (2) the build direction, and (3) the application of HT. Fig. 6a–c demonstrate the increases in the tensile strengths of the conventional, composite, and hybrid composite structures, respectively, which were obtained due to (1) the intrinsically high strengths of the reinforcements, (2) the strong bonding between the matrix and reinforcement phases, and (3) the Hall–Petch strengthening provided from the grain size reduction through the prevention of the grain growth in the matrix by the reinforcements [12,30,43]. Furthermore, although the complementary and synergistic effects of the SiC and nitride reinforcements in the Mg_2Si matrix were present, the microscale SiC affected the tensile strength (a bulk property) more than the nanoscale nitrides owing to

the smaller sizes and lower concentrations of the latter. The LPBF-processed structures along the vertical and horizontal directions were compared. The primary drawback of LPBF-based AM is the occurrence of increased mechanical flaws (e.g., pores, cracks, and fractures) from the longer processing time and more extensive overlap of the powder during AM along the vertical direction relative to that along the horizontal direction [19]. Furthermore, although HT endowed all the structures with nearly isotropic tensile strengths, irrespective of their build directions, the strain differences could not be entirely overcome because of the remaining mechanical flaws—even after the active solid-solution treatment at a high temperature of 800 °C [19]. Similarly, the compression testing results of the conventional, composite, and hybrid composite structures have been presented, as shown in Fig. 6d–f, which are identical to the previous tensile testing results. For the hybrid composite prior to HT, the FEM (Figure S7) was used to computationally verify the equivalent stress concentrations at the SiC and nitride reinforcements, but more dominantly at the SiC reinforcement, due to (1) the presence of SiC with a significantly greater size and (2) the embedment of SiC at the melt pools, which resisted the concentration of external stress more effectively than did the nitrides with the fan-shaped distributions along the melt pools, even though the latter provided extensive stress resistance [12,30,43]. Fig. 6g–i present the weight differences before and after wear testing, changes in COF, and wear depths of the nonreinforced, composite, and hybrid composite structures before and after HT. Initially, all of the COF values decreased abruptly from a minimum of –1.20 to a maximum of –1.86 within 50 s due to the initial contact, and then stabilized somewhat (with weak fluctuations) for the remainder of the test. Before HT, the particularly high COF values of the conventional, composite, and hybrid composite structures resulted in intensive abrasion and active scratching of the surfaces in tribological contact, which generated focused pull-out junctions as the shear force increased [12,30,43]. In detail, prior to HT, the hybrid composite surface exhibited intensive abrasion and active scratching of the surfaces in tribological contact due to the specific distribution of the nanoscale nitrides, which generated focused pull-out junctions as the shear force increased. With respect to the microstructure, the SiC reinforcement was present along with the melt pools in the Mg_2Si matrix. Furthermore, the nitride compounds were distributed from the centers to the edges of the melt pools, in line with the fan shape of the melt pools, owing to the exposure to N_2 gas during laser irradiation. After HT, however, the slippery and lubricating effects became slightly more dominant, with more stabilized COF values, during identical tribology testing [20,21]. In the wear depth measurements, the graphs were rapidly saturated, thereby revealing their actual values after the polished surfaces of the structures were sufficiently worn by the counterface WC bead [18,19]. The wear depth is strongly affected by the shear strength of a composite structure and disproportional to the presence and concentration of the reinforcement in the matrix. Meanwhile, although large undulations were present in both the COF and wear depth graphs due to the
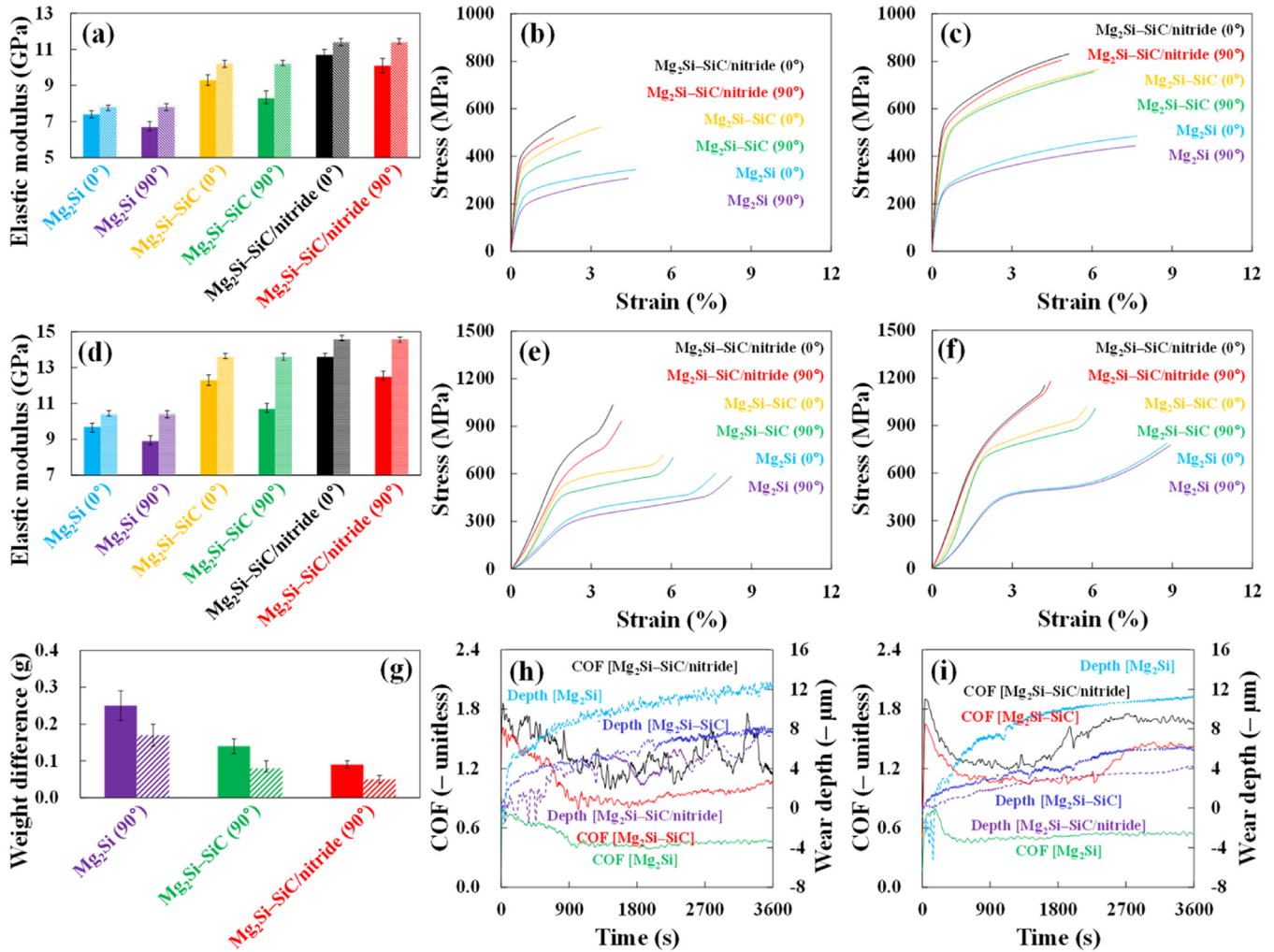
Fig. 6. (a, b, d, e) Before HT, the mechanical strengths increased in the order of the Mg_2Si structure < the Mg_2Si–SiC composite < the Mg_2Si–SiC/nitride hybrid composite, while the strains decreased in the same order, due to the reinforcement effects of the SiC and nitrides inside the Mg_2Si matrix. (a, c, d, f) After HT, the mechanical strengths and strains of all three structures were enhanced owing to (1) the alleviation of the residual and thermal stresses in the Mg_2Si matrix generated by laser irradiation and (2) the reduction of the crystalline defects and mechanical flaws at the interfacial boundaries between the Mg_2Si, SiC, and nitrides. (g–i) The wear resistance increased in all three structures due to the reinforcement effects in accordance with the tensile and compression testing results.

presence of nitrides prior to HT, these became significantly smoother after HT, mainly due to removal of the defects and flaws, along with dispersion of the nitrides, although the hybrid composite dually reinforced with the SiC and nitrides contributed to improving the anti-friction and wear resistance performances.

3.6. Additive manufacturing of a pinion-and-rack steering gear system that fulfills the effective structural stiffness and specific material-strengthening performance requirements

We conducted a case study for the topological optimization of a pinion and rack as the core parts used in a steering gear system to demonstrate the practical feasibility of the new type of hybrid composite (Fig. 7). First, the original pinion consisted of a combination of as-cast components. It was subsequently subjected to forging and 45 cycles of machin-

ing. Moreover, the pinion had a complicated round sawtooth with a 60° angle on the top to sustain high wear resistance when in contact with the sawtooth plate of the rack. A long round stick in the middle and a docking loop on the bottom were designed to resist the shear force (500 N), which was controlled using an electronic signal. Subsequently, the rack requires identical pre- and post-processing. It comprises a sawtooth plate on the simple round bar structure transferring the applied pressure (0.2 MPa) to the sawtooth of the pinion, which was directly interconnected to the handle of a vehicle. For topological optimization, we analyzed the equivalent stress distribution on the force and pressure when the external load interacted with each part at a unique orientation while excluding any structural deformation of the entire structure for compliance minimization (stiffness maximization) [17,44–46]. The geometric boundary was divided according to the topological optimization rule, and the maximum equivalent stress
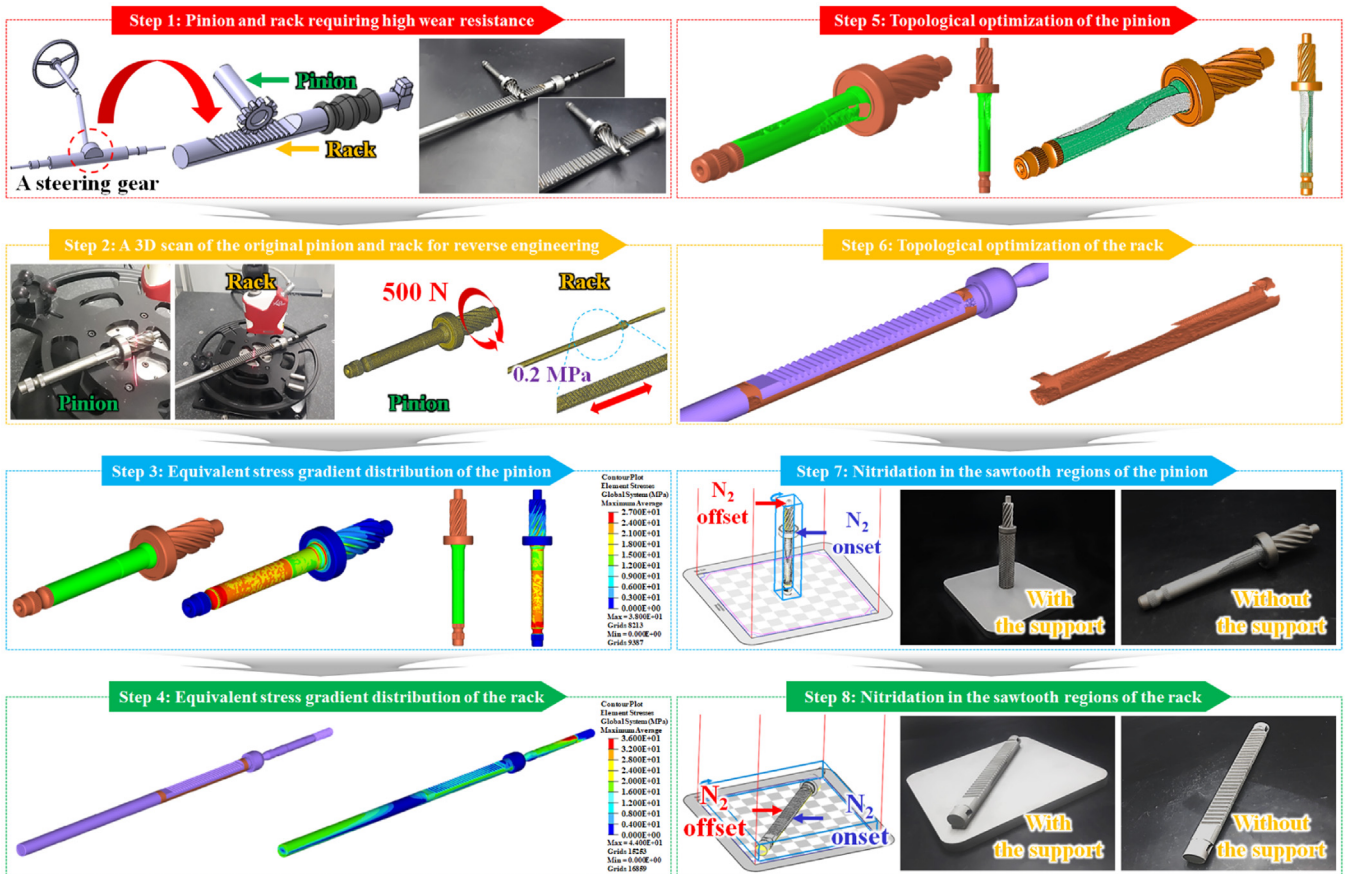
Fig. 7. Step 1: Schematics showing the geometries and photographs of the pinion and rack in the steering gear before topological optimization. In particular, the sawtooth regions of the pinion and rack required strong wear resistance because fracturing of the steering gear system is a direct safety threat to the driver. Step 2: Photographs and schematics showing the geometries of the two original steering gear parts 3D-scanned for reverse engineering. Steps 3 and 4: The equivalent stress gradient distributions of the pinion and rack in response to a shear force of 500 N and push pressure of 0.2 MPa, respectively, to identify both the solid and potentially topologically optimizable (removable) areas prior to AM in the next step. Steps 5 and 6: The ergonomic geometries of the pinion and rack after topological optimization for stiffness maximization and weight minimization of the parts, which were subjected to the maximum equivalent stress levels of 168.2 and 172.1 MPa along the vertical and horizontal directions, respectively. The applied stress levels are, respectively, one-third of the corresponding directional yield strengths of the Mg_2Si–SiC composite (504.6 and 516.3 MPa, respectively) after AM of the parts with weight reductions exceeding 22.5% and 19.3%, respectively. Steps 7 and 8: In addition to applying the mechanical stiffness-increasing mechanism through the topological optimization of the two steering gear parts, the nitridation of the specific components (i.e., the sawtooth regions and regions in their vicinity) further improved their strength based on the material-strengthening mechanism.

was found to be one-third of the yield strength (168.2 MPa) based on the previous tensile testing result of the aged composite structure (additively manufactured along the vertical direction). Furthermore, the volume reduction was maximized until the safety factor became 3.0. Thus, from a structural perspective, the newly designed parts sufficiently surpassed the required mechanical stiffness and deformation resistance.

Although the topologically optimized pinion and rack parts were constructed predominantly of a structurally stable solid, the mechanical stiffness can be improved in direct correlation with driver safety. Thus, inside the topologically optimized pinion, a lattice structure was adopted with a double helix shape and hatching distance of 800 µm, as depicted in Step 5 of Fig. 7. As a result, utilization of the cellular structure inside the topologically optimized pinion provided a considerably higher safety factor of 3.5 (an increase of 0.5 compared to the safety factor of the topologically optimized part without

the cellular structure), which immediately increased the mechanical stiffness and minimized the material usage, despite retention of the overhang design to increase the fuel efficiency of the vehicle used herein [14,47]. It was topologically optimized for the rack until having a safety factor of 3.5, even without the cellular structure regarding driver safety as the priority. However, although topological optimization of the two parts can ensure that each part has the required adequate volume while the entire structure has the lowest weight possible, specifically targeting each desired region in these parts is a complex endeavor. Furthermore, considering this geometric perspective, it is impossible to increase the strength of only the sawtooth and adjacent regions through a structural transformation. In particular, because the sawtooth regions for both the pinion and rack require even higher wear resistance than that from the SiC reinforcement in the Mg_2Si matrix, the nitridation becomes an auxiliary and effective

strengthening technique considering the material. Meanwhile, because the nitridation occurred only during laser irradiation under N_2, the primary structural design and support structure alignment should be carefully considered when applying the material-strengthening mechanism during AM, especially along the build direction. In addition to applying the mechanical stiffness-increasing mechanism through the topological optimization (shape and geometry transformation) of the two steering gear parts, the nitridation of the specific components (the sawtooth regions and regions in their vicinity) further improved their strength based on the material-strengthening mechanism. Consequently, one can combine topological optimization with the material-strengthening mechanism by considering the geometric characteristic and composite material, respectively, in addition to adopting the lattice structure for the auxiliary strength to maximize mechanical stiffness (minimize structural deformation) and, ultimately, effective wear resistance.

4. Conclusion

The high wear resistance of the Mg_2Si–SiC/nitride hybrid composite was provided by the reinforcement effects of the multi-modal compounds (i.e., the dual *ex-situ* incorporated SiC micropowder and *in-situ* incorporated nitride nanoparticles) embedded in the Mg_2Si matrix. In particular, the nitride compounds were distributed over the microstructure from the centers to the edges of the melt pools, due to the formation of a CGD owing to the gradual exchange of N_2 in Ar during laser irradiation. The LPBF process created an FGS in the intended regions when constructing a pinion-and-rack steering gear system with the requisite high wear resistance, thus demonstrating the feasibility of the AM process for this new type of hybrid composite. Consequently, before heat treatment, the tensile strength and coefficient of friction of the AMed hybrid composite were 569.0 MPa and –1.13, respectively, compared to 344.1 MPa and –0.47, for the AMed non-reinforced (conventional) structure. Moreover, after heat treatment, these values were significantly enhanced to 831.5 MPa and –1.67 for the hybrid composite compared to 485.3 MPa and –0.54 for the conventional structure. Based on this approach, the two automobile parts were fabricated by following the tenets of AM to identify the possibility of the practical (even commercial) use of the steering gear system in a high-performance vehicle.

Data availability

All the research data supporting this publication are directly available within this publication, even though this manuscript has been published as open access.

Declaration of competing interest

The authors declare no competing interests.

CRediT authorship contribution statement

Jeongho Yang: Formal analysis, Conceptualization. **Woongbeom Heogh:** Software, Formal analysis, Conceptualization. **Sukhyun Kang:** Supervision, Formal analysis, Conceptualization. **Tae-Sik Jang:** Validation, Investigation, Conceptualization. **Hyun-Do Jung:** Investigation, Funding acquisition, Conceptualization. **Seung Chul Han:** Resources, Investigation, Conceptualization. **Seong Je Park:** Validation, Investigation, Conceptualization. **Young Won Kim:** Supervision, Investigation, Conceptualization. **Clodualdo Aranas Jr.:** Writing – review & editing, Writing – original draft, Software, Methodology, Funding acquisition, Conceptualization. **Sang Hoon Kim:** Writing – original draft, Supervision, Investigation, Formal analysis, Conceptualization.

Supplementary materials

Supplementary material associated with this article can be found, in the online version, at doi:10.1016/j.jma.2024.03.008.

References

[1] G. Wu, K.C. Chan, L. Zhu, L. Sun, J. Lu, Nature 545 (2017) 80–83.
[2] C. Liu, Y. Ji, J. Tang, K. Otsuka, Y. Wang, M. Hou, Y. Hao, S. Ren, P. Luo, T. Ma, D. Wang, X. Ren, Nat. Mater. 21 (2022) 1003–1007.
[3] W. Xu, N. Birbilis, G. Sha, Y. Wang, J.E. Daniels, Y. Xiao, M. Ferry, Nat. Mater. 14 (2015) 1229–1235.
[4] M. Esmaily, J.E. Svensson, S. Fajardo, N. Birbilis, G.S. Frankel, S. Virtanen, R. Arrabal, S. Thomas, L.G. Johansson, Prog. Mater. Sci. 89 (2017) 92–193.
[5] X. Dong, M. Xia, F. Wang, H. Yang, G. Ji, E.A. Nyberg, S. Ji, J. Magnes. Alloy. 11 (2023) 2939–2952.
[6] G. Proust, Science 365 (2019) 30–31.
[7] Z. Wu, R. Ahmad, B. Yin, S. Sandlöbes, W.A. Curtin, Science 359 (2018) 447–452.
[8] L.Y. Chen, J.Q. Xu, H. Choi, M. Pozuelo, X. Ma, S. Bhowmick, J.M. Yang, S. Mathaudhu, X.C. Li, Nature 528 (2015) 539–543.
[9] B.Y. Liu, F. Liu, N. Yang, X.B. Zhai, L. Zhang, Y. Yang, B. Li, J. Li, E. Ma, J.F. Nie, Z.W. Shan, Science 365 (2019) 73–75.
[10] A. Bandyopadhyay, K.D. Traxel, M. Lang, M. Juhasz, N. Eliaz, S. Bose, Mater. Today 52 (2022) 207–224.
[11] K.B. Nie, X.J. Wang, K.K. Deng, X.S. Hu, K. Wu, J. Magnes. Alloy. 9 (2021) 57–77.

[12] Y. Lakhdar, C. Tuck, J. Binner, A. Terry, R. Goodridge, Prog. Mater. Sci. 116 (2021) 100736.

[13] J.H. Martin, B.D. Yahata, J.M. Hundley, J.A. Mayer, T.A. Schaedler, T.M. Pollock, Nature 549 (2017) 365–369.

[14] G. Liu, X. Zhang, X. Chen, Y. He, L. Cheng, M. Huo, J. Yin, F. Hao, S. Chen, P. Wang, S. Yi, L. Wan, Z. Mao, Z. Chen, X. Wang, Z. Cao, J. Lu, Mater. Sci. Eng. R 145 (2021) 100596.

[15] C. Zhang, Z. Li, J. Zhang, H. Tang, H. Wang, J. Magnes. Alloy. 11 (2023) 425–461.

[16] S.H. Kim, H. Lee, S.M. Yeon, C. Aranas, K. Choi, J. Yoon, S.W. Yang, H. Lee, Addit. Manuf. 47 (2021) 102288.

[17] D. Gu, X. Shi, R. Poprawe, D.L. Bourell, R. Setchi, J. Zhu, Science 372 (2021) eabg1487.

[18] D. Raabe, C.C. Tasan, E.A. Olivetti, Nature 575 (2019) 64–74.

[19] S.H. Kim, S.M. Yeon, J.H. Lee, Y.W. Kim, H. Lee, J. Park, N.K. Lee, J.P. Choi, C. Aranas, Y.J. Lee, S. An, K. Choi, Y. Son, Virtual Phys. Prototyp. 15 (2020) 460–480.

[20] T.S. Jang, S.J. Park, J.E. Lee, J. Yang, S.H. Park, M.B.G. Jun, Y.W. Kim, C. Aranas, J.P. Choi, Y. Zou, R.C. Advincula, Y. Zheng, H.L. Jang, N.J. Cho, H. Do Jung, S.H. Kim, Adv. Funct. Mater. 32 (2022) 2206863.

[21] S.H. Kim, G.H. Shin, B.K. Kim, K.T. Kim, D.Y. Yang, C. Aranas, J.P. Choi, J.H. Yu, Sci. Rep. 7 (2017) 1–13.

[22] Z. Sun, W. Guo, L. Li, Addit. Manuf. 33 (2020) 101175.

[23] S.A. Khairallah, A.A. Martin, J.R.I. Lee, G. Guss, N.P. Calta, J.A. Hammons, M.H. Nielsen, K. Chaput, E. Schwalbach, M.N. Shah, M.G. Chapman, T.M. Willey, A.M. Rubenchik, A.T. Anderson, Y.M. Wang, M.J. Matthews, W.E. King, Science 368 (2020) 660–665.

[24] Y.S. Lee, W. Zhang, Addit. Manuf. 12 (2016) 178–188.

[25] H.L. Wei, T. Mukherjee, W. Zhang, J.S. Zuback, G.L. Knapp, A. De, T. DebRoy, Prog. Mater. Sci. 116 (2021) 100703.

[26] R. Shi, S.A. Khairallah, T.T. Roehling, T.W. Heo, J.T. McKeown, M.J. Matthews, Acta Mater. 184 (2020) 284–305.

[27] C. Ghosh, C. Aranas, J.J. Jonas, Prog. Mater. Sci. 82 (2016) 151–233.

[28] M.S. Pham, C. Liu, I. Todd, J. Lertthanasarn, Nature 565 (2019) 305–311.

[29] M. Benedetti, A. du Plessis, R.O. Ritchie, M. Dallago, N. Razavi, F. Berto, Mater. Sci. Eng. R 144 (2021) 100606.

[30] L.Y. Chen, S.X. Liang, Y. Liu, L.C. Zhang, Mater. Sci. Eng. R 146 (2021) 100648.

[31] A. Bandyopadhyay, K.D. Traxel, S. Bose, Mater. Sci. Eng. R 145 (2021) 100609.

[32] T.C. Lin, C. Cao, M. Sokoluk, L. Jiang, X. Wang, J.M. Schoenung, E.J. Lavernia, X. Li, Nat. Commun. 10 (2019) 1–9.

[33] K.D. Traxel, A. Bandyopadhyay, Addit. Manuf. 24 (2018) 353–363.

[34] F. Wang, P. Altschuh, A.M. Matz, J. Heimann, B.S. Matz, B. Nestler, N. Jost, Acta Mater. 170 (2019) 138–154.

[35] P. Kürnsteiner, M.B. Wilms, A. Weisheit, B. Gault, E.A. Jägle, D. Raabe, Nature 582 (2020) 515–519.

[36] T. DebRoy, T. Mukherjee, H.L. Wei, J.W. Elmer, J.O. Milewski, Nat. Rev. Mater. 6 (2021) 48–68.

[37] M. Laleh, E. Sadeghi, R.I. Revilla, Q. Chao, N. Haghdadi, A.E. Hughes, W. Xu, I. De Graeve, M. Qian, I. Gibson, M.Y. Tan, Prog. Mater. Sci. 133 (2022) 101051.

[38] S.C. Yoo, D. Lee, S.W. Ryu, B. Kang, H.J. Ryu, S.H. Hong, Prog. Mater. Sci. 132 (2022) 101034.

[39] S. Gantenbein, K. Masania, W. Woigk, J.P.W. Sesseg, T.A. Tervoort, A.R. Studart, Nature 561 (2018) 226–230.

[40] M. Imai, Y. Isoda, H. Udono, Intermetallics 67 (2015) 75–80.

[41] Z. Li, R.C. Bradt, J. Am. Ceram. Soc. 69 (1986) 863–866.

[42] T. DebRoy, H.L. Wei, J.S. Zuback, T. Mukherjee, J.W. Elmer, J.O. Milewski, A.M. Beese, A. Wilson-Heid, A. De, W. Zhang, Prog. Mater. Sci. 92 (2018) 112–224.

[43] X. Li, L. Lu, J. Li, X. Zhang, H. Gao, Nat. Rev. Mater. 5 (2020) 706–723.

[44] B.E. Carroll, R.A. Otis, J.P. Borgonia, J.O. Suh, R.P. Dillon, A.A. Shapiro, D.C. Hofmann, Z.K. Liu, A.M. Beese, Acta Mater. 108 (2016) 46–54.

[45] M. Sokoluk, C. Cao, S. Pan, X. Li, Nat. Commun. 10 (2019) 1–8.

[46] A. du Plessis, S.M.J. Razavi, M. Benedetti, S. Murchio, M. Leary, M. Watson, D. Bhate, F. Berto, Prog. Mater. Sci. 125 (2021) 100918.

[47] M. Zhang, N. Zhao, Q. Yu, Z. Liu, R. Qu, J. Zhang, S. Li, D. Ren, F. Berto, Z. Zhang, R.O. Ritchie, Nat. Commun. 13 (2022) 3247.

[48] L.K. Pillari, K. Lessoway, L. Bichler, J. Magnes. Alloy. 11 (2023) 1825–1905.